A Readout IC for Capacitive Touch Screen Panels With 33.9 dB Charge-Overflow Reduction Using Amplitude-Modulated Multi-Frequency Excitation

An, Jae Sung; Ra, Jong Hyun; Kang, Eunchul; Pertijs, Michiel A.P.; Han, Sang Hyun

DOI
10.1109/JSSC.2021.3100470

Publication date
2021

Document Version
Final published version

Published in
IEEE Journal of Solid-State Circuits

Citation (APA)
An, J. S., Ra, J. H., Kang, E., Pertijs, M. A. P., & Han, S. H. (2021). A Readout IC for Capacitive Touch Screen Panels With 33.9 dB Charge-Overflow Reduction Using Amplitude-Modulated Multi-Frequency Excitation. *IEEE Journal of Solid-State Circuits*, *56*(11), 3486-3498. https://doi.org/10.1109/JSSC.2021.3100470

A Readout IC for Capacitive Touch Screen Panels With 33.9 dB Charge-Overflow Reduction Using Amplitude-Modulated Multi-Frequency Excitation

Jae-Sung An, *Member, IEEE*, Jong-Hyun Ra, Eunchul Kang, *Member, IEEE*,
Michiel A. P. Pertijs, *Senior Member, IEEE*, and Sang-Hyun Han

***Abstract*—This article presents a readout integrated circuit (ROIC) for capacitive touch-screen panels (TSPs) employing an amplitude-modulated multiple-frequency excitation (AM-MFE) technique. To prevent charge overflow, which occurs periodically at the beat frequency of the excitation frequencies, the ROIC modulates the amplitude of the excitation voltages at a mixing frequency derived from the excitation frequencies. Thus, the ROIC can sense the charge signal without charge overflow and maximize the signal-to-noise ratio (SNR) by increasing the amplitude of the excitation voltages up to the sensing range of the readout circuit. The proposed ROIC was fabricated in a 0.13-μm standard CMOS process and was measured with a 32-in 104 × 64 touch-screen panel using 1 and 10 mm metal pillars. It reduces charge overflow up to 33.9 dB compared to operation without AM-MFE. In addition, the ROIC achieves a frame rate of 2.93 kHz, and SNRs of 41.7 and 61.6 dB with 1 and 10 mm metal pillars, respectively.**

***Index Terms*—Amplitude-modulated multi-frequency excitation (AM-MFE), capacitive touch system (CTS), charge overflow reduction, frame rate, readout IC (ROIC), signal-to-noise ratio (SNR), touch screen panel (TSP).**

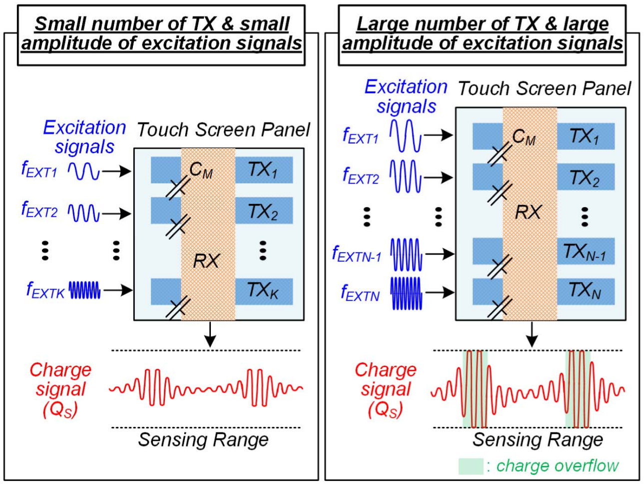

Fig. 1. Conceptual diagram illustrating charge overflow.

I. INTRODUCTION

AMONG several types of touch systems [1]–[35], capacitive touch systems (CTSs) [6]–[35] are widely used in various applications, such as smart watches, smart phones, tablet PCs, desktop PCs, and interactive white boards, because of their capability to support multi-touch expression, their high sensitivity, their durability, and their optical transparency [5], [6]. To sense the fast movements of a finger and fine stylus, the readout integrated circuit (ROIC) should have a high frame rate and a high signal-to-noise ratio (SNR). To satisfy these requirements, several parallel transmitter (TX) driving methods, such as multi-frequency and coded excitation, have been proposed [19]–[32]. However, the ROIC cannot sense the charge signal (Q_S) during the charge-overflow periods that occur when it drives a large number of TX electrodes with large-amplitude excitation signals, as shown in Fig. 1 [30].

To solve the charge overflow, several methods have been proposed [21], [25], [27]–[30]. The charge-signal cancellation method [21] avoids charge overflow by inducing a compensation signal at the receiver (RX) readout circuit to cancel Q_S during the charge overflow period, but it is hard not only to synchronize with Q_S but also to control the amplitude of the compensation signal accurately. The parallel TX driving method avoids charge overflow for a small number of TX electrodes and excitation signals [25], but it results in low SNR and low frame rate. Reducing the amplitude of the excitation signal [18], [27] avoids charge overflow, but it also degrades the SNR. The parallel TX driving method with modified orthogonal matrices [30] can alleviate the charge overflow.

Manuscript received December 12, 2020; revised February 9, 2021, April 8, 2021, May 31, 2021, and July 18, 2021; accepted July 18, 2021. Date of publication August 5, 2021; date of current version October 22, 2021. This article was approved by Associate Editor Pui-In Mak. *(Corresponding author: Jae-Sung An.)*

Jae-Sung An and Michiel A. P. Pertijs are with the Electronic Instrumentation Laboratory, Delft University of Technology, 2628 CD Delft, The Netherlands (e-mail: jaesungan0629@hotmail.com).

Jong-Hyun Ra is with SK Hynix Inc., Icheon-si, Gyeonggi 17336, South Korea.

Eunchul Kang was with the Electronic Instrumentation Laboratory, Delft University of Technology, 2628 CD Delft, The Netherlands. He is now with Sony Semiconductor Solutions, 1366 Lysaker, Norway.

Sang-Hyun Han is with Leading UI Company, Ltd., Anyang, Gyeonggi 14057, South Korea.

Color versions of one or more figures in this article are available at https://doi.org/10.1109/JSSC.2021.3100470.

Digital Object Identifier 10.1109/JSSC.2021.3100470

However, this method is not suitable for a large number of TX electrodes because it still suffers from charge overflow. The signal omitting and linear interpolation method [28] prevents charge overflow by ignoring Q_S during the period of charge overflow and reconstructing it using interpolation in the digital domain, but it results in a heavy computational load in the digital back-end part.

Differential sensing is another approach that has been taken to prevent charge overflow, with the added benefit that it also reduces errors due to common-mode interfering signals. Fully-differential amplifiers and multiplexers have been employed to generate an output voltage proportional to the difference in mutual capacitance (C_M) between adjacent RX electrodes [12], [24], [31]. However, this approach reduces the frame rate by a factor of two, because the sensing direction is periodically switched between even and odd RX electrodes to detect the touch point. Moreover, it leads to a reduction in signal level, because each RX electrode connects to two input stages, causing the signal current to divide between them. To remove the common signal (Q_S and noise) without frame rate and signal-level degradation, many ROICs have used the differential sensing at the output of charge amplifiers, integrators, and filters, but then these front-end circuits still suffer from the charge overflow at the input node [16], [21], [23].

To prevent charge overflow without degrading frame rate, SNR, and computational load, this article proposes an ROIC employing amplitude-modulated multi-frequency excitation (AM-MFE). This technique is based on the observation that charge overflow occurs at the beat frequency of the excitation frequencies. A microcontroller unit (MCU) decides a mix frequency (f_{MIX}) derived from this beat frequency. To reduce the amplitude of the excitation signals with the same periodicity, the excitation signals that drive the TX electrodes of the touch screen panel (TSP) are amplitude-modulated at f_{MIX}. The readout circuit receives the resulting charge signals from the TSP without the charge overflow. Thus, the readout circuit maintains the frame rate, while maximizing the charge-signal amplitude up to the sensing range to improve SNR. Experimental results are presented that demonstrate the functionality of the proposed ROIC as well as the effectiveness of the AM-MFE in combination with a 32-in 104 × 64 TSP using 1 and 10 mm metal pillars.

This article is organized as follows. Section II describes the system architecture of the CTS. Sections III and IV describe the proposed AM-MFE and ROIC, respectively. In Section V, the experimental results are evaluated and compared with previous work. Finally, the conclusion is given in Section VI.

II. ARCHITECTURE OF THE CTS

Fig. 2(a) and (b) show a block diagram of the CTS using the proposed AM-MFE and the associated excitation and charge signals, respectively. The proposed CTS consists of the TSP, MCU, and ROIC including the M-channel readout and N-channel excitation circuits, and a fast Fourier transform (FFT) processor.

To achieve a high SNR, the MCU first finds a low-noise frequency region in the FFT without driving the TX electrodes, and locates the N excitation frequencies (f_{EXT1} to f_{EXTN}) in this low-noise frequency region [26], [27]. In addition, the MCU derives f_{MIX} from the distribution of f_{EXT1} to f_{EXTN}. When the excitation circuit receives f_{EXT1} to f_{EXTN} and f_{MIX} from the MCU, it generates the excitation signals amplitude-modulated at f_{MIX} to drive the TX electrodes. The resulting Q_S sensed by the readout circuit has the constant amplitude rather than overflowing periodically. To maximize the SNR, the ROIC increases the amplitude of Q_S up to the sensing range of the readout circuit by increasing the amplitude of the excitation signals. The readout circuit digitizes the charge signals and transfers the resulting analog-to-digital converter (ADC) data to the FFT processor. The FFT processor extracts the FFT data (D_{FFT}) representing the frequency spectrum of Q_S, and sends it to the MCU [26], [27]. This allows the MCU to detect the touch coordinates without heavy computational load, as will be detailed in Sections III-B and V.

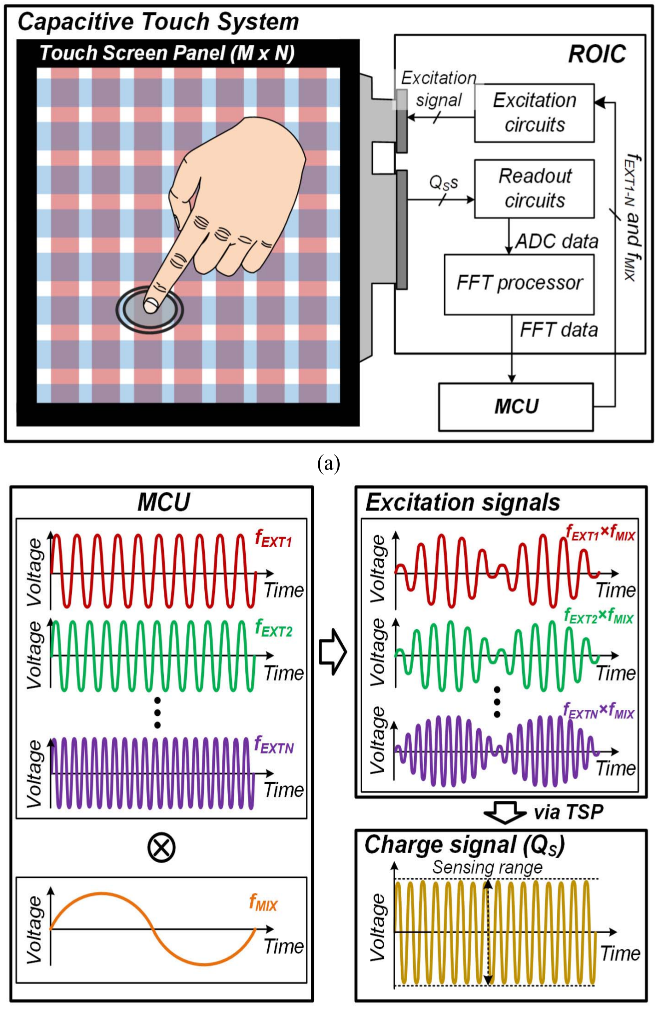

(a)

(b)

Fig. 2. (a) Block diagram of the CTS with proposed AM-MFE and (b) its signals.

III. ANALYSIS OF THE AM-MFE TECHNIQUE

A. Conventional Multi-Frequency Excitation (MFE)

Conventional MFE can achieve high SNR and high frame rate [26], [27]. However, as the number of TX electrodes

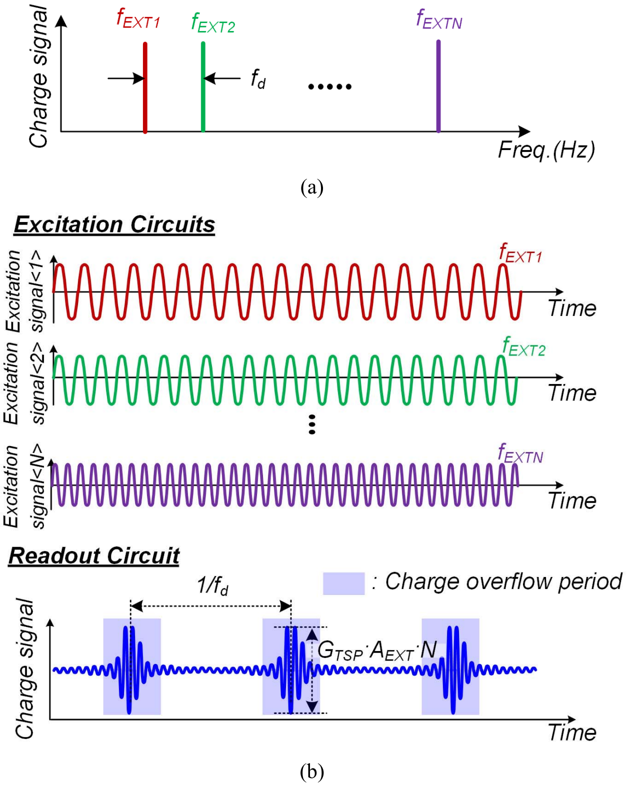

Fig. 3. Conventional MFE in (a) frequency and (b) time domains.

or the excitation amplitude are increased, the charge-signal amplitude increases proportionally and can exceed the sensing range. To avoid such charge overflow, the amplitude can be reduced, or a subset of the TX electrodes can be driven with a large amplitude, but this degrades SNR and frame rate, respectively [26], [27].

To simplify the analysis of the relationship among the amplitude of the charge-signal ($Q_{S,\text{MFE}}$), the number of TX electrodes N, and the excitation-signal amplitude A_{EXT}, the excitation frequencies f_{EXT1} to f_{EXTN} are assumed to be spread equidistantly at a fixed interval f_d, as shown in Fig. 3(a). When the excitation circuits simultaneously drive the TX electrodes, the Q_S can be written as follows:

$$Q_{S,\text{MFE}}(t) = G_{\text{TSP}} \cdot \sum_{0}^{N-1} A_{\text{EXT}} \cdot \sin(2\pi (f_{\text{EXT1}} + i \cdot f_d) \cdot t) \quad (1)$$

where G_{TSP} is the conversion gain of the TSP. For the TSP used in our design, G_{TSP} (measured with an Agilent/HP 4284A precision LCR meter) was 1.680 pF, and its variation (ΔG_{TSP}) due to a 10-mm metal pillar touch was 0.134 pF. As illustrated in Fig. 3(b), this signal periodically peaks when all sinusoidal terms constructively add, leading to a peak amplitude of $G_{\text{TSP}} \times A_{\text{EXT}} \times N$ that occurs at time interval of $1/f_d$.

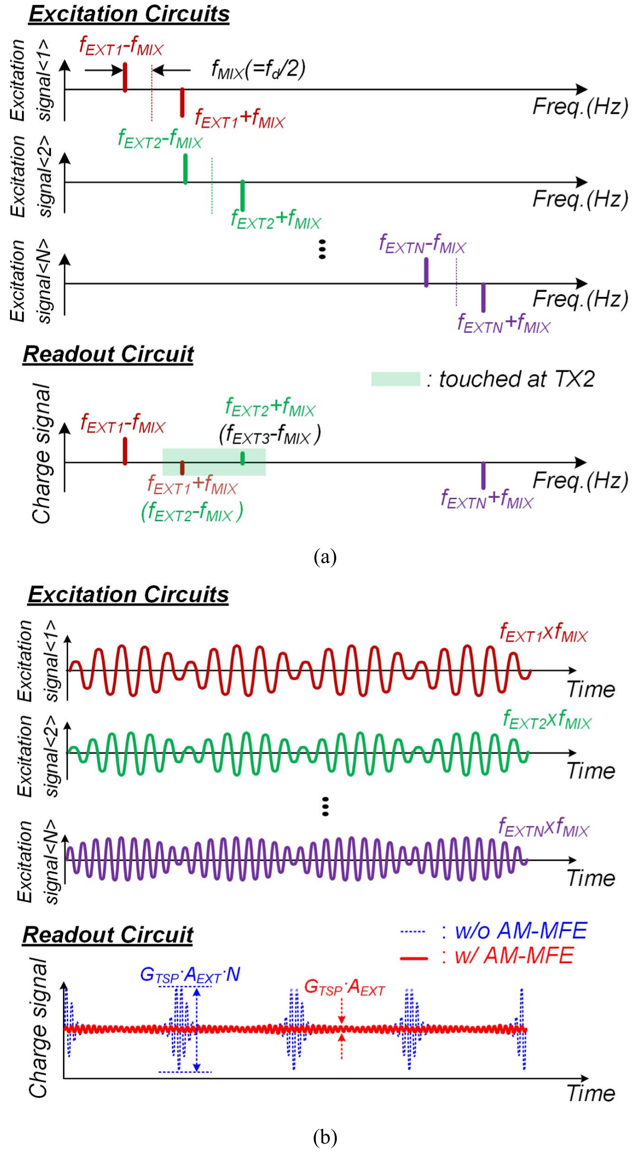

Fig. 4. Conceptual diagrams of the proposed AM-MFE in (a) frequency and (b) time domains.

B. Proposed AM-MFE

Fig. 4(a) and (b) show the conceptual diagrams of the proposed AM-MFE in the frequency and time domains, respectively. The excitation circuit modulates the amplitude of the excitation signals with a sinusoidal signal at f_{MIX}. The resulting Q_S sensed by the readout circuit equals

$$Q_{S,\text{AM-MFE}}(t) = Q_{S,\text{MFE}}(t) \cdot \sin(2\pi \cdot f_{\text{MIX}} \cdot t). \quad (2)$$

When the MCU sets f_{MIX} to $f_d/2$ [see Fig. 2(a)], (2) can be re-expressed as follows:

$$\begin{aligned} &Q_{S,\text{AM-MFE}}(t) \\ &= G_{\text{TSP}} \cdot \sum_{0}^{N-1} A_{\text{EXT}} \cdot \sin\left(2\pi \left(f_{\text{EXT1}} + i \cdot f_d\right) \cdot t\right) \cdot \sin(\pi \cdot f_d \cdot t) \\ &= G_{\text{TSP}} \cdot A_{\text{EXT}} \cdot \sum_{0}^{N-1} \\ &\quad \times \left[\frac{-1}{2}\left\{\cos\left(2\pi\left(f_{\text{EXT1}} + \left(i + \frac{1}{2}\right) \cdot f_d\right) \cdot t\right)\right.\right. \\ &\qquad \left.\left. - \cos\left(2\pi\left(f_{\text{EXT1}} + \left(i - \frac{1}{2}\right) \cdot f_d\right) \cdot t\right)\right\}\right] \end{aligned}$$

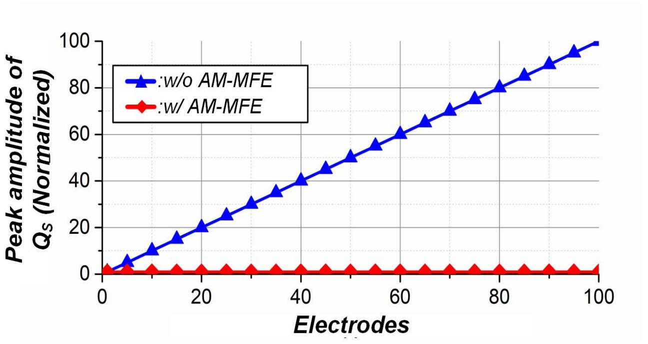

Fig. 5. Simulated peak amplitude of the charge signal as a function of the number of TX electrodes, with and without the proposed AM-MFE.

$$= \cdots = \frac{G_{\mathrm{TSP}} \cdot A_{\mathrm{EXT}}}{2} \cdot \left\{ \cos\left(2\pi t\left(f_{\mathrm{EXT1}} - \frac{f_d}{2}\right)\right) - \cos\left(2\pi t\left(f_{\mathrm{EXTN}} + \frac{f_d}{2}\right)\right)\right\}. \quad (3)$$

Referring to Fig. 4, this expression shows that the Q_S from TX electrode i is split into two components $f_{\mathrm{EXTi}} \pm f_{\mathrm{MIX}}$ with an opposite polarity and half amplitude. Since the charge signals from all TX electrodes add together, all components from $f_{\mathrm{EXT1}} + f_{\mathrm{MIX}}$ to $f_{\mathrm{EXTN}} - f_{\mathrm{MIX}}$ cancel out (assuming all capacitance are nominally equal), and only two components at $f_{\mathrm{EXT1}} - f_{\mathrm{MIX}}$ and $f_{\mathrm{EXTN}} + f_{\mathrm{MIX}}$ remain. In the time domain, this results in much less amplitude variation, due to the fact the amplitude-modulation of the excitation signals prevents the periodic peaking of the amplitude of the Q_S, as shown in Fig. 4(b).

When a finger touches the TSP, for instance, on the second TX electrode, additional components at $f_{\mathrm{EXT1}} + f_{\mathrm{MIX}}$ (or $f_{\mathrm{EXT2}} - f_{\mathrm{MIX}}$) and $f_{\mathrm{EXT2}} + f_{\mathrm{MIX}}$ (or $f_{\mathrm{EXT3}} - f_{\mathrm{MIX}}$) are added. These additional components represent the touch information, and can be easily detected by the MCU to extract the touch coordinates without the heavy computational load.

Referring to (3), noting that the value of two cosines ranges from -1 to 1, the peak amplitude of $Q_{S,\mathrm{AM\text{-}MFE}}(t)$ is only determined by $A_{\mathrm{EXT}} \cdot G_{\mathrm{TSP}}$. Therefore, the proposed ROIC using the AM-MFE can prevent the charge overflow regardless of the number of TX electrodes. Rather than using equidistant excitation frequencies, f_{EXT1} to f_{EXTN} can be assigned having the prime number frequency spacing to minimize the frequency interference among frequencies them. In this case, the MCU derives the f_{MIX} from the histogram of f_ds among $f_{\mathrm{EXT1}} - f_{\mathrm{EXTN}}$. This will be explained in detail in Section V.

Fig. 5 shows the simulated peak amplitude of the Q_S as a function of the number of TX electrodes. The proposed AM-MFE successfully prevents the charge overflow regardless of the number of TX electrodes, allowing the ROIC to send a large-amplitude excitation signal to all TX electrodes in any number of TX electrodes.

IV. PROPOSED ROIC

Fig. 6 shows a block diagram of the proposed ROIC. It consists of N-channel excitation circuits, M-channel readout circuits, an FFT processor, and an interface to the MCU. The excitation circuit includes for each channel a direct digital synthesizer (DDS), a low-pass filter (LPF), a mixer, and a programmable gain amplifier (PGA), as well as mixer controller shared by all channels. The readout circuit, for each channel, consists of a second-generation current conveyor (CCII), a high-pass filter (HPF), and 4:1 multiplexers (MUXs) and ADCs.

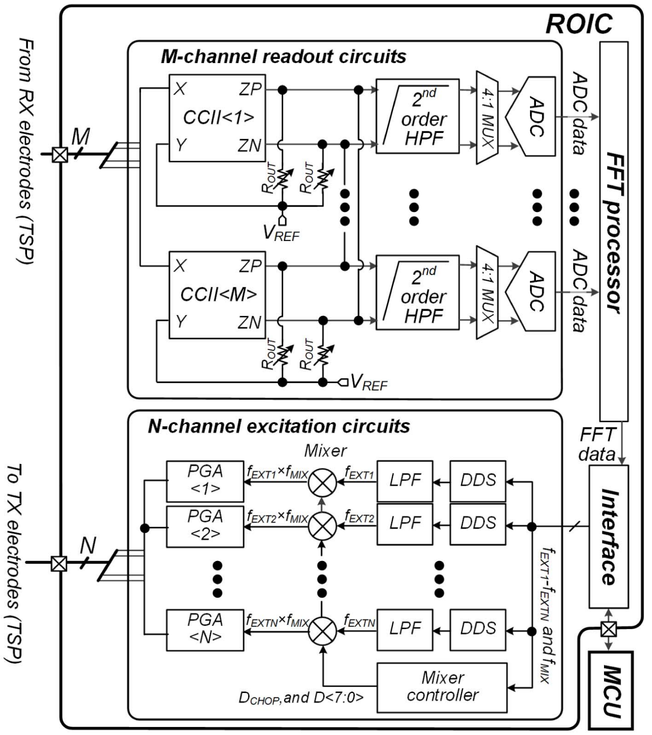

Fig. 6. Block diagram of the proposed ROIC.

A. Excitation Circuits

The excitation circuit receives f_{EXT1} to f_{EXTN} and f_{MIX} from the MCU via the interface. To generate the sinusoidal signals having different frequencies within a small die area, DDSs are used [36], [37], which generate control data for 4-bit digital-to-analog converters (DACs) that approximate the sinusoidal signals ($V_{\mathrm{DDS,OUT}}$) with discrete voltage steps [27]. To filter out out-of-band signals and harmonics each DDS is followed by a first-order LPF. Furthermore, the cut-off frequencies of these LPFs is adaptively adjusted according to f_{EXT1} to f_{EXTN}. The output of the LPF (V_{LPF}) drives the mixer.

Fig. 7(a) and (b) show the schematic and timing diagrams of the mixer, which includes a chopper amplifier and mixing capacitors (C_{MIX1} and C_{MIX2}) and 2:1 multiplexers. The chopper amplifier consists of an operational amplifier and two chopper switches, which are controlled by D_{CHOP}. The gain of the mixer is set by the ratio $C_{\mathrm{MIX1}}/C_{\mathrm{MIX2}}$, where the value of C_{MIX1} is determined by the mixer controller using $D\langle 7{:}0\rangle$. The polarity of the gain is determined by the multiplexers and chopper switches. When the D_{CHOP} is high, the mixer has an inverting configuration. When the D_{CHOP} is low, the mixer has a non-inverting configuration. Thus, the mixer can generate an amplitude-modulated output V_{MIX}

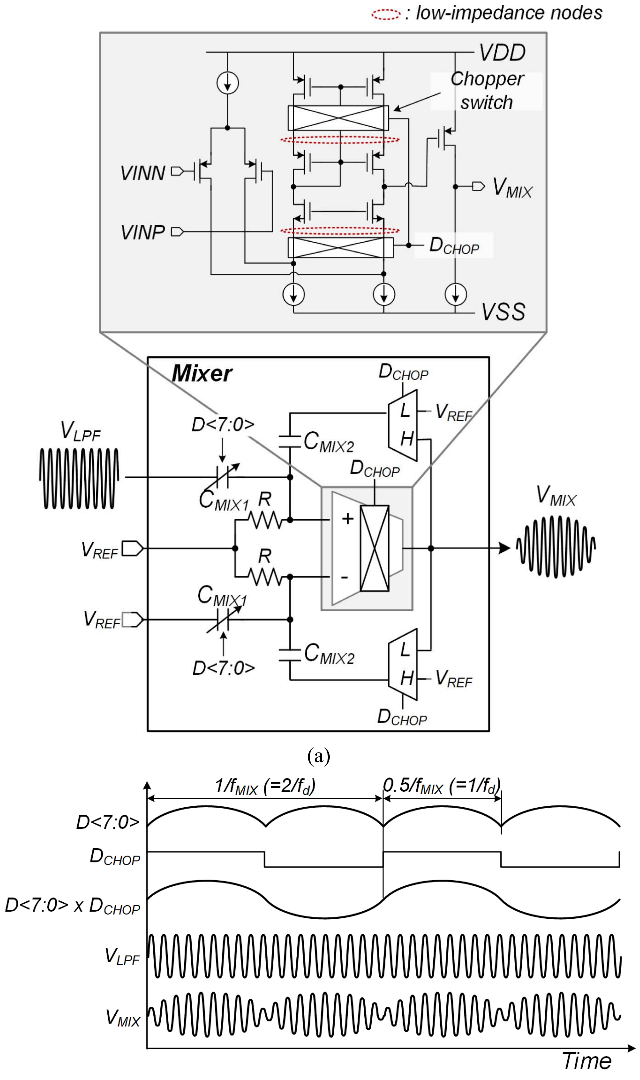

(a)

(b)

Fig. 7. (a) Schematic and (b) timing diagrams of the mixer.

from the combination of $D\langle 7{:}0\rangle$ and D_{CHOP}. To minimize the voltage ripple of V_{MIX} because of the switching operation, the two chopper switches are placed at the low impedance nodes in the operational amplifier [17], [38], [39]. After the mixer, the PGA provides programmable gain and drives the TX electrode [26], [27], [40].

B. Readout Circuits and FFT Processor

The ROIC suffers from external interference from the display panel, switched-mode power supply, and florescent lamp, which degrade the SNR [16], [27]. To filter out such interference within a small die area, a differential sensing method is implemented at the output of a CCII-based input stage [19], [27], [29]. (It is noted that we do not implement differential sensing directly at the input to avoid the reduction in frame rate and signal level associated with such an implementation, as discussed in Section I.)

Fig. 8 shows the schematic and timing diagram of the readout circuit using a CCII, a differential sensing enable switch (EN_DIFF), a second-order HPF, a 4:1 MUX, and a 12-bit successive-approximation (SAR) ADC. In the CCII, which contains two input ports (X and Y) and two output ports (ZP and ZN), the ports X and Y of are connected to the Kth channel RX electrode and a reference voltage (V_{REF}), respectively. Because the operational amplifier and MOSFETs (M_{P1} and M_{N1}) from a negative feedback loop [27], the RX electrode is thus biased at V_{REF}. The Q_S is induced into port X as a current I_X, which is mirrored through the M_{P2}–M_{P6}, giving current I_{ZP}, and also mirrored through the M_{N2}–M_{N6}, giving current I_{ZN} whose current direction is opposite to I_{ZP}. Since I_{ZP} and I_{ZN} flow through the output resistors (R_{OUT}), the output voltages are given by as follows:

$$\begin{aligned} V_{\text{OUTP,CCII}} &= V_{\text{REF}} + R_{\text{OUT}} \times I_{\text{ZP}} \\ V_{\text{OUTN,CCII}} &= V_{\text{REF}} - R_{\text{OUT}} \times I_{\text{ZN}}. \end{aligned} \tag{4}$$

The amplitudes of $V_{\text{OUTP,CCII}}$ and $V_{\text{OUTN,CCII}}$ are adaptively controlled by adjusting the value of R_{OUT}, without using an additional capacitor array, which would occupy a large area [27].

To realize the differential sensing method using the CCII, the ports ZP and ZN of the Kth channel CCII (CCII$\langle K\rangle$) are connected with the port ZN of $(K-1)$th channel CCII (CCII$\langle K-1\rangle$) and port ZP of $(K+1)$th channel CCII (CCII$\langle K+1\rangle$), respectively, by closing the EN_DIFF switch (EN_DIFF $= 1$). When the EN_DIFF switch is disconnected (EN_DIFF $= 0$), the ROIC is set to the single-channel sensing method [27]. Since the currents at the ZP and ZN ports are added, the resulting differential output voltages at ports ZP and ZN of CCII$\langle K\rangle$ are

$$\begin{aligned} V_{\text{OUTP,CCII}}\langle K\rangle &= V_{\text{REF}} + R_{\text{OUT}} \times (I_{\text{ZP}}\langle K\rangle - I_{\text{ZN}}\langle K-1\rangle) \\ V_{\text{OUTN,CCII}}\langle K\rangle &= V_{\text{REF}} - R_{\text{OUT}} \times (I_{\text{ZN}}\langle K\rangle - I_{\text{ZP}}\langle K+1\rangle) \end{aligned} \tag{5}$$

where $I_{\text{ZP}}\langle K\rangle$, $I_{\text{ZN}}\langle K\rangle$, $I_{\text{ZN}}\langle K-1\rangle$, and $I_{\text{ZP}}\langle K+1\rangle$ are currents at port ZP of CCII$\langle K\rangle$, port ZN of CCII$\langle K\rangle$, port ZN of CCII$\langle K-1\rangle$, and port ZP of CCII$\langle K+1\rangle$, respectively.

When a finger touches the TSP, for instance, on the cross-point of the second TX and the Kth RX electrodes, the capacitance C_M at the touched point is changed by factor of α ($\alpha < 1$). From (3), when the gain of all CCIIs is set to A_{CCII}, $i_{\text{ZP}}\langle K\rangle$ and $i_{\text{ZN}}\langle K-1\rangle$ can be expressed as follows:

$$i_{\text{ZP}}\langle K\rangle = \frac{A_{\text{CCII}} \cdot G_{\text{TSP}} \cdot A_{\text{EXT}}}{2} \cdot \left\{ \begin{array}{c} \cos\left(2\pi t\left(f_{\text{EXT1}} - \frac{f_d}{2}\right)\right) - (1-\alpha) \\ \times \cos\left(2\pi t\left(f_{\text{EXT1}} + \frac{f_d}{2}\right)\right) \\ +(1-\alpha) \times \cos\left(2\pi t\left(f_{\text{EXT2}} + \frac{f_d}{2}\right)\right) \\ -\cos\left(2\pi t\left(f_{\text{EXTN}} + \frac{f_d}{2}\right)\right) \end{array} \right\} \tag{6}$$

and

$$\begin{aligned} &i_{\text{ZN}}\langle K-1\rangle \\ &= -\frac{A_{\text{CCII}} \cdot G_{\text{TSP}} \cdot A_{\text{EXT}}}{2} \\ &\quad \cdot \left\{\cos\left(2\pi t\left(f_{\text{EXT1}} - \frac{f_d}{2}\right)\right) - \cos\left(2\pi t\left(f_{\text{EXTN}} + \frac{f_d}{2}\right)\right)\right\} \end{aligned} \tag{7}$$

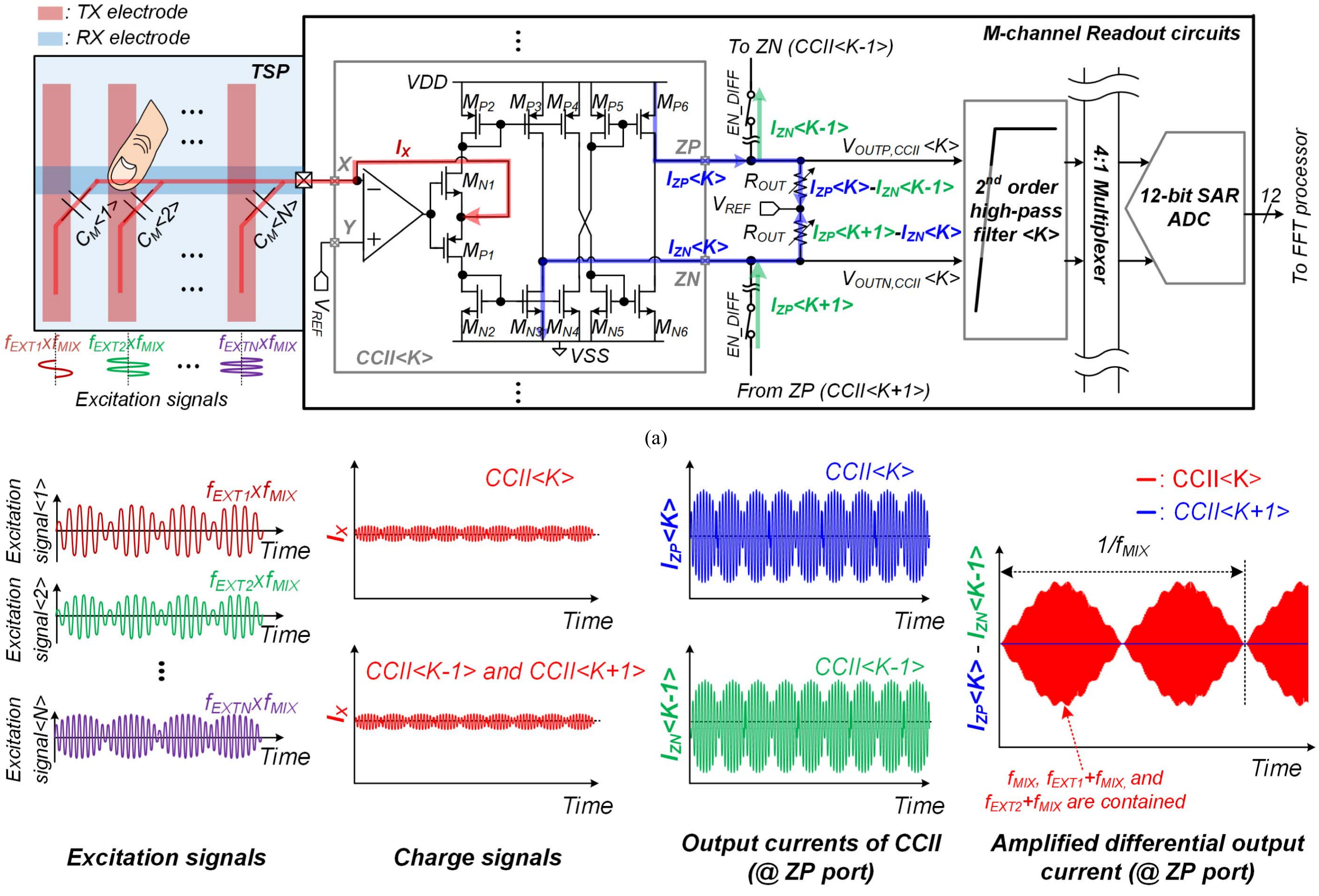

Fig. 8. (a) Schematic of the M-channel readout circuits and (b) timing diagram.

respectively. Since the finger only touches the cross-point of the second TX and the Kth RX electrodes, $i_{\mathrm{ZN}}\langle K-1\rangle$ only has components at $f_{\mathrm{EXT1}} - f_d/2$ and $f_{\mathrm{EXTN}} + f_d/2$. In contrast, $i_{\mathrm{ZP}}\langle K\rangle$ has additional components at $f_{\mathrm{EXT1}} + f_d/2$ (or $f_{\mathrm{EXT2}} - f_d/2$), and $f_{\mathrm{EXT2}} + f_d/2$ (or $f_{\mathrm{EXT3}} - f_d/2$). As shown in Fig. 8, due to the connection of the ZN port of CCII$\langle K-1\rangle$ to the ZP port of CCII$\langle K\rangle$, $i_{\mathrm{ZN}}\langle K-1\rangle$ flows from the ZP port of CCII$\langle K\rangle$ to the ZN port of CCII$\langle K-1\rangle$, thus canceling out the common components. The remaining current ($i_{\mathrm{ZP}}\langle K\rangle - i_{\mathrm{ZN}}\langle K-1\rangle$) at CCII$\langle K\rangle$ that flows into R_{OUT} can be expressed as follows:

$$\begin{aligned}
&i_{\mathrm{ZP}}\langle K\rangle - i_{\mathrm{ZN}}\langle K-1\rangle\\
&\quad= \frac{A_{\mathrm{CCII}}\cdot G_{\mathrm{TSP}}\cdot A_{\mathrm{EXT}}}{2}\\
&\qquad\cdot\left\{-(1-\alpha)\times\cos\left(2\pi t\left(f_{\mathrm{EXT1}}+\frac{f_d}{2}\right)\right)+(1-\alpha)\right.\\
&\qquad\quad\left.\times\cos\left(2\pi t\left(f_{\mathrm{EXT2}}+\frac{f_d}{2}\right)\right)\right\}.
\end{aligned}\tag{8}$$

Which has components at f_{EXT1}, f_{EXT2}, and $f_d/2$, and represents the touch point. The current at the port ZN of CCII$\langle K\rangle$ is similar but has an opposite current direction.

In contrast, the differential output current at an untouched RX electrode (e.g., the $(K+1)$th RX electrode) is ideally zero (when all C_Ms are same). Moreover, any external interference, which leads to a signal that is common between neighboring channels, is removed with a simple circuit structure. Any residual interference is suppressed by the combination of the TSP and the CCII, which operates as a first-order bandpass filter (BPF) [26], [27], and a second-order HPF filter.

As the 32-in TSP used in this work has a 1.5-MHz cut-off frequency, the excitation frequencies f_{EXT1} to f_{EXTN} can be located up to 1.5 MHz. To meet the Nyquist criterion, $V_{\mathrm{OUTP,CCII}}$ and $V_{\mathrm{OUTN,CCII}}$ should be sampled at 3 MHz. To do so, a 12-bit SAR ADC with a 12 MHz sampling rate ($f_{\mathrm{ADC,SAMPLE}}$) is shared by 4 CCII and HPF channels by means of a 4:1 multiplexer. The ADC is operated asynchronously to eliminate the need for an external oversampled clock, which would increase the complexity of the ROIC [41], [42]. The ADC's output data are fed to an FFT processor, which converts them to 1024-point output data D_{FFT} distributed from −1.5 to 1.5 MHz [27]. The frame rate of the proposed ROIC (f_{ROIC}) can be derived using

$$f_{\mathrm{ROIC}} = \frac{f_{\mathrm{ADC,SAMPLE}}}{N_{\mathrm{CCII,ADC}}\times N_{\mathrm{FFT}}}\tag{9}$$

where $N_{\mathrm{CCII,ADC}}$ and N_{FFT} are the number of channels of the CCII per ADC and the number of points in the FFT processor [27]. Since the proposed ROIC using AM-MFE can simultaneously drive all TX electrodes, f_{ROIC} is maintained to be 2.93 kHz. In addition, it achieves a high SNR with small die area because of the differential sensing method with CCIIs.

V. EXPERIMENTAL RESULTS

Fig. 9(a) shows the measurement setup of the proposed CTS with a 32-in 104 × 64 TSP. To have small resistance, the TX and RX electrodes are made of copper wire, which has a metal width of 10.0-μm and a sheet resistance of less than 4.0 $\Omega/\square$. In addition, to prevent bending, the TSP is covered with a 3.0-mm-thick cover glass. To measure the proposed CTS, a full-high-definition liquid crystal display is placed under the TSP with a 2.0 mm air gap in between. The TSP is connected with the ROIC board through flexible printed circuit boards (FPCBs). The ROIC board is controlled by the MCU board and a PC via cables.

To be able to demonstrate the potential of the proposed techniques with excitation amplitudes beyond what the current ROIC can provide, 64 high-voltage amplifiers (OPA455 [43]) were mounted on the board between the ROIC and the TSP. As shown in Fig. 9(b), a non-inverting amplifier configuration is used to increase the amplitude of the excitation signal. By adjusting the ratio of R1 and R2, the amplitude of excitation signal can be adjusted from 10 to 150 V.

Fig. 9(c) shows the display noise spectrum, measured on the TSP via a 10-mm diameter metal pillar. The noise is concentrated in the frequency range from 80 to 250 kHz. By considering this frequency spectrum, the touch sensing system locates the excitation frequencies in the low-noise region.

Fig. 9(d) shows a photomicrograph of the ROIC, which was fabricated in a 0.13-μm standard CMOS process. It includes 104 readout channels, 64 excitation circuits, an FFT processor, and peripheral and interface circuitry. It occupies an area of 8500 μm × 8500 μm and uses a 256-pin ball grid array package.

Fig. 10 shows the simulated common-mode rejection ratio (CMRR) of the differential sensing method, obtained using a 1000-iteration Monte Carlo mismatch simulation. The simulated CMRR ranges from 41 to 106 dB, with a mean value of 57.7 dB and a standard deviation of 10.4 dB. To extract the touch coordinate, the MCU subtracts the touch data (touch signal + mismatch signal) from the baseline data (mismatch signal) with a gain compensation. Moreover, the touch data are averaged in the MCU to match the frame rate of the touch controller with the display (60 or 120 Hz). Thus, output offset due to finite CMRR does not significantly affect the touch coordinate extraction.

Table I and Fig. 11 show the measurement conditions to compare the performance with and without the proposed AM-MFE technique. As shown in Table I, the excitation frequencies f_{EXT1} to f_{EXT64} are located from 298.86 to 655.34 kHz, respectively, at an equidistant frequency spacing of 5.86 kHz, and thereby f_{MIX} is set to the 2.93 kHz. Alternatively, when f_{EXT1} to f_{EXT64} are not evenly distributed (e.g., prime number frequency spacing), f_{MIX} can be determined

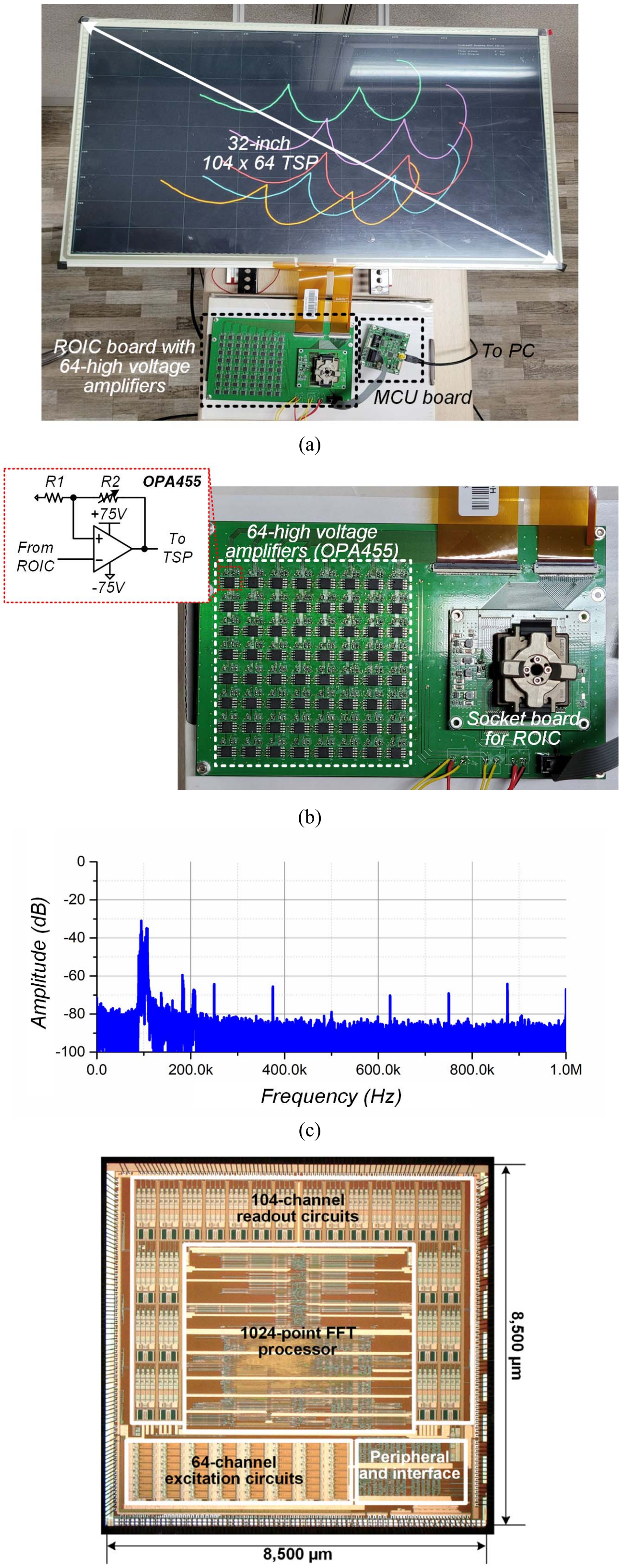

(a)

(b)

(c)

(d)

Fig. 9. (a) Measurement setup of the capacitive touch system. (b) ROIC board with HV amplifiers (OPA455 [43]). (c) Display noise. (d) Photomicrograph of the ROIC.

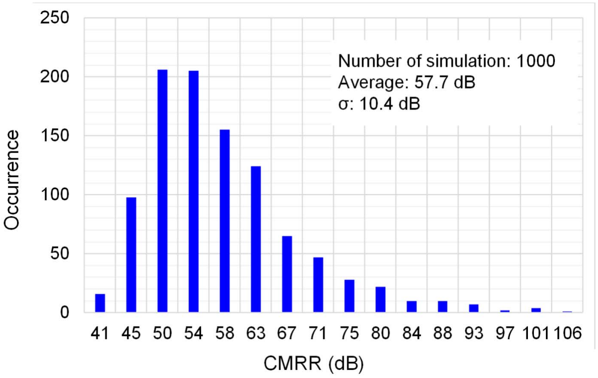

Fig. 10. Monte Carlo mismatch simulation of differential output signals.

TABLE I

MEASUREMENT CONDITION OF THE PROPOSED CTS

Number of electrodes		104 × 64
Excitation Frequencies	f_{EXT1} (kHz)	286.16 kHz
	f_{EXT64} (kHz)	655.34 kHz
	f_d (kHz)	5.86 kHz
	f_{MIX} (kHz)	2.93 kHz

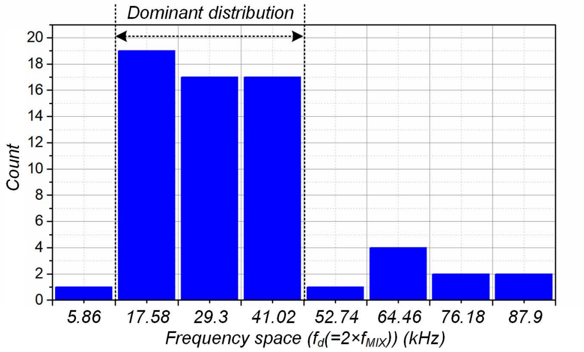

Fig. 11. Frequency histogram for extracting of f_{MIX} in the prime f_d (f_{EXT1} is set to 286.86 kHz).

based on a histogram of the frequency intervals. As shown in Fig. 10, the largest interval is 87.9 kHz implying that f_{MIX} can be set to 43.95 kHz. However, to reduce power consumption, the MCU set f_{MIX} based on the dominant intervals in the histogram, and decides the f_{MIX}s among the 8.79, 14.65, and 20.51 kHz.

To demonstrate the reduction in signal amplitude achieved by the proposed AM-MFE technique, one would ideally like to probe the charge signal at the input node of the CCII. Because this is not directly accessible, Fig. 12 shows, instead, the output data of the 12-bit ADC for a fixed value of the CCII's output resistance R_{OUT} and with differential sensing disabled, i.e., EN_DIFF $= 0$ [see Fig. 8(a)]. Under these conditions, the charge-signal amplitude reduction can achieve by AM-MFE can be evaluated through the amplitude reduction observed at the ADC output.

As shown in Fig. 12(a), for an excitation amplitude of 3.3 V, the ADC output codes range between 297 and 3789 when AM-MFE is not used, because of the superposition of excitation signals. On the other hand, when the AM-MFE is used with equidistant frequency spacing, the ADC output codes range between 2012 and 2082, showing that the AM-MFE reduces the amplitude by 33.9 dB. (It is noted that under normal operation, R_{OUT} would not be fixed, as in this experiment, but adaptively adjusted to make better use of the ADC's dynamic range in the AM-MFE case).

As shown in Fig. 12(b), for a 10 V excitation amplitude, applied with the help of the external high-voltage amplifiers, the ADC output code saturates when the AM-MFE is not used. When the AM-MFE is used, the ADC output codes range between 1955 and 2146. As shown in Fig. 12(c), for a 140 V excitation amplitude, the ADC output code also saturates when the AM-MFE is not used. When the AM-MFE is used, the ADC output codes range between 216 and 3906.

For the case of prime-number frequency spacing and an excitation amplitude of 3.3 V, as shown in Fig. 12(d), the ADC output codes range between 582 and 3513 when the AM-MFE is not used. With AM-MFE is used, with f_{MIX} of 8.79 kHz, this is reduced to 1329 and 2909, i.e., a 5.9 dB improvement. These reductions in amplitude by AM-MFE can reduce charge overflow, and thereby the ROIC can enhance SNR by increasing the excitation amplitude up to 33.9 dB.

Fig. 13 shows, for the case of the prime-number frequency spacing using the AM-MFE, the measured ADC data for different values of f_{MIX}. For increase values of f_{MIX}, the amplitude decreases up to 20.51 kHz, and then fluctuates because of interference between the excitation frequencies and f_{MIX} in the ROIC. This shows that f_{MIX} can be selected from the frequency range from 8.79 to 43.95 kHz.

Fig. 14 shows the measured FFT data for the case of equidistant frequency spacing (see Table I), both when the TSP is untouched, and when a 1 mm metal pillar is placed on the TSP. When the TSP is not touched, only two components at 283.23 kHz (286.16 – 2.93 kHz) and 658.27 kHz (286.16 + 2.93 kHz) are visible, since the intermediate components cancel out, as discussed in Section III-B. When the screen is touched, additional components appear, which represent the touched electrodes and its adjacent electrodes. Using this information, the MCU can extract the touch coordinates. When the external noise is applied to TSP through the touch object with a frequency of 300–600 kHz, for instance, the MCU first finds a low-noise frequency region by means of the FFT processor without driving the TX electrodes, and locates the excitation frequencies in the low-noise frequency region (avoiding the frequency range of 300–600 kHz). Therefore, despite the in-band noise, the ROIC and MCU can detect the touch point without influencing from the external noise.

Fig. 15 shows a 3-D representation of the D_{FFT} data for the complete 32-in 104×64 TSP. The location of 1 and 10 mm metal pillars can be successfully extracted from this, showing proper operation of the CTS with the AM-MFE.

Fig. 16(a) and (b) show the measured SNRs without and with AM-MFE, respectively, for equidistant frequency spacing ($f_d = 5.86$ kHz). The SNR of the CTS is calculated, according

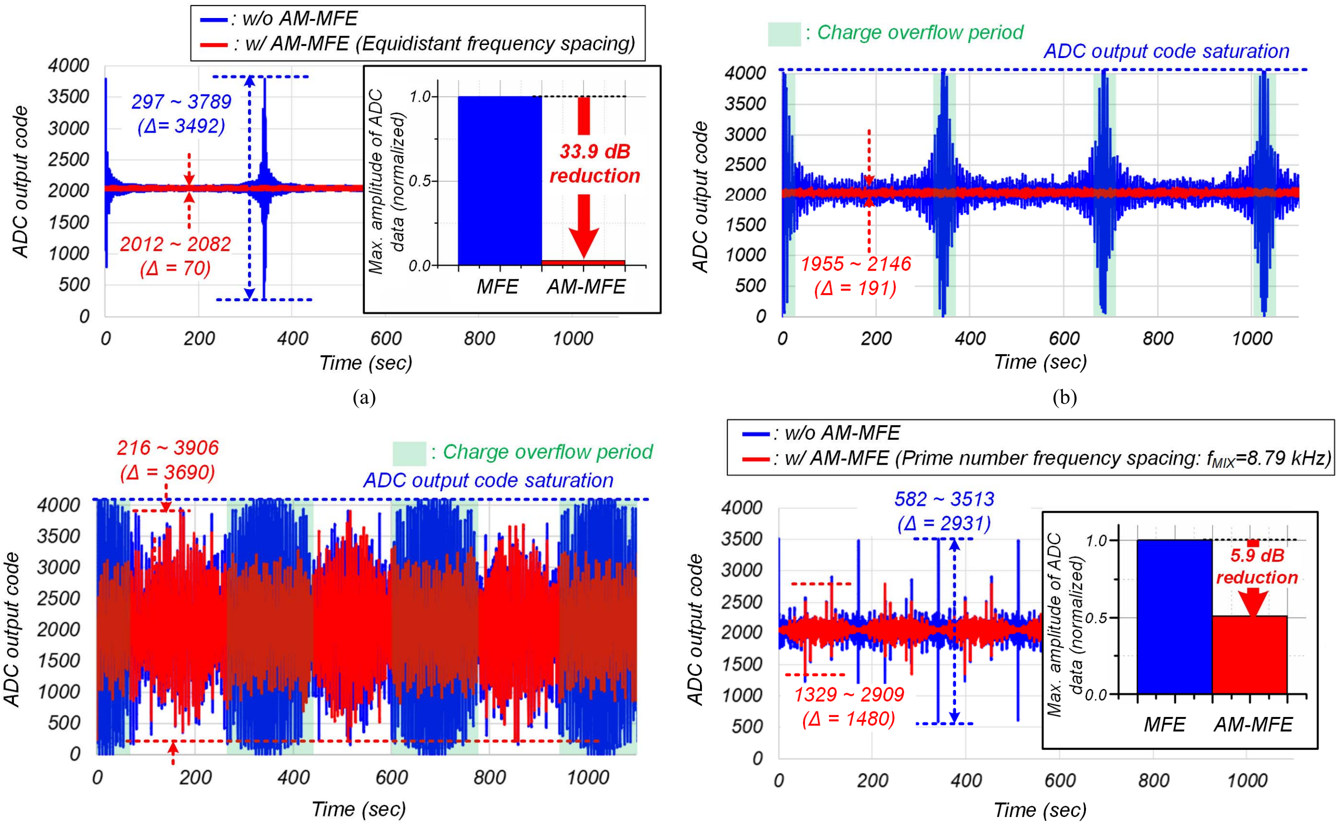

(a) (b)

(c) (d)

Fig. 12. Measured ADC data for (a) equidistant frequency spacing with 3.3 V excitation signal, (b) equidistant spacing with 10 V excitation signal, (c) equidistant spacing with 140 V excitation signal, and (d) prime-number spacing with 3.3 V excitation signal ($f_{\mathrm{MIX}} = 8.79$ kHz).

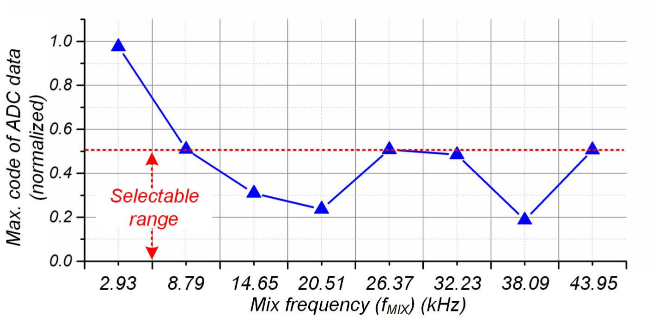

Fig. 13. Measured normalized ADC data amplitude as a function of f_{MIX} for prime-number frequency spacing using the AM-MFE.

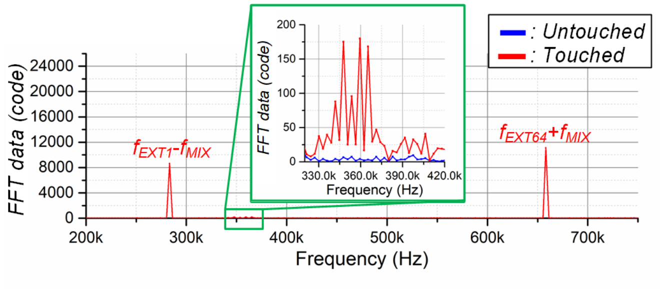

Fig. 14. Measured frequency spectra with equidistant frequency spacing.

the approach used in [16], [18], [19], [26], as follows:

$$\mathrm{SNR(dB)} = 20 \times \log\left(\frac{S_{\mathrm{TOUCH}}}{N_{\mathrm{RMS}}}\right) \tag{10}$$

where the rms noise level is calculated based on the standard deviation of 100 FFT readings $D_{\mathrm{FFT,Touch}}$ in the touched condition, i.e.,

$$N_{\mathrm{RMS}} = \sqrt{\frac{\sum_{n=0}^{99}\left\{D_{\mathrm{FFT,Touch}}[n] - \left(\sum_{m=0}^{99}\frac{D_{\mathrm{FFT,Touch}}[m]}{100}\right)\right\}^2}{100}} \tag{11}$$

and the signal level S_{TOUCH} is the average value of the difference in the 100 FFT readings between the touched and untouched conditions. It is noted that each of the FFT readings is calculated based on a large number of ADC readings ($N_{\mathrm{FFT}} = 1024$), and hence the ADC is effectively oversampled, and an SNR higher than 74 dB can be achieved.

The differential sensing method removes the common noise and common signal [12], [24], [31]. However, in the proposed ROIC, the differential sensing method is done at the output node of CCII, the charge overflow at the input node of CCII is still existing. To solve this, the proposed AM-MFE reduces the charge overflow at the input node of CCII. After then, the differential sensing method also removes the common noise and remaining common signal at the output node of CCII.

TABLE II

PERFORMANCE SUMMARY OF THE PROPOSED CTS IN COMPARISON WITH PREVIOUS WORKS

		This work	ISSCC 2014 [21]	JSSC 2016 [25]	JSSC 2018 [18]	JSSC 2018 [27]	ISSCC 2018 [28]	ISSCC 2018 [29]	JSSC 2019 [30]
Process		**0.13-µm CMOS**	0.18-µm CMOS	0.18-µm CMOS	0.18-µm CMOS	0.13-µm CMOS	100-nm CMOS	0.13-µm CMOS	0.18-µm CMOS
TSP size		**32-inch**	4.8-inch	10.1-inch	10.1-inch	65-inch	10.1-inch	86-inch	12.2-inch
# of electrodes		**104 × 64**	24 × 16	48 × 32	50 × 28	104 × 64	54 × 35	198 × 112	64 × 36
Electrode		**Metal Mesh**	N/A	ITO	N/A	Metal Mesh	Metal mesh	Metal mesh	ITO
Frame rate		**2.93 kHz**	160 Hz	240 Hz	120 Hz	3.9 kHz	133 Hz	977 Hz	85~385 Hz
Charge overflow reduction method		**AM-MFE**	Q_S cancellation method at the charge overflow period	Time dividing method	Decreasing the amplitude of excitation signal	Decreasing the amplitude of excitation signal	Linear interpolation method	Time dividing method	Modified orthogonal matrices
Maximum charge overflow reduction ratio		**33.9 dB**	N/A	N/A	N/A	N/A	N/A	6.02 dB	13.98 dB
SNR	Metal pillar (Φ=1mm)	**41.7 dB (equidistant) 41.2 dB (prime-number)**	N/A	49.0 dB	40.4 dB	41.0 dB	56.0 dB	39.0 dB	41.0 dB (@120 Hz frame rate)
	Finger	**61.6 dB[1] (equidistant) 85.5 dB[3] (equidistant, 140V excitation signal) 61.1 dB[1] (prime-number)**	53 dB	62.0 dB (Φ=6 mm)	53.3 dB	61.0 dB (Φ=10 mm)	N/A	60.1 dB (Φ=10 mm)	54.0 dB (@120 Hz frame rate)
Supply		**1.5 / 3.3 / 5.0 V**	1.8 / 3.3V	N/A	1.8 / 3.3V	1.5 / 3.3 V	N/A	1.5 / 3.3 V	2.7~3.3V
Power consumption		**290.8 mW (@5V excitation signal)**	2.6 mW (Analog)	30 mW	6.9 mW	246.3 mW	24.0 mW	797.4 mW	94.5 mW (@3.3V) 67.7 mW (@1.8/3.3V)
FoM (pJ/step)[2]		**15.2 (@5V excitation signal)**	115.9	353.4	108.7	10.3	185.2	44.5	489.7
Chip area		**72.25 mm^2**	0.46 mm^2	14.7 mm^2	1.96 mm^2	42.25 mm^2	39.2 mm^2	74.17 mm^2	36.0mm^2

[1] 10mm metal pillar

[2] FoM=Power consumption / ($2^{(\text{SNR}-1.76)}$/6.02 × # of node × frame rate) [18]

[3] Measured using an external amplifier to provide a high excitation voltage [43].

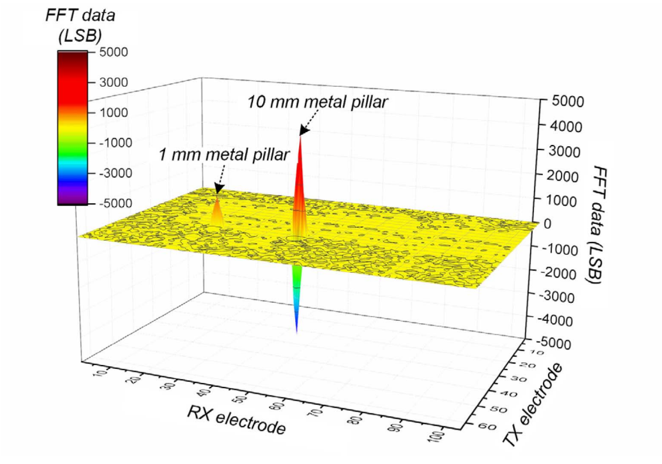

Fig. 15. Coordinate extraction for the 1- and 10-mm metal pillars.

Without AM-MFE, the ROIC cannot increase the SNR by increasing the excitation amplitude because of the charge overflow at the input node of CCII. With AM-MFE, the excitation amplitude can be increased up to 5 V, limited by the supply voltage of the ROIC. To demonstrate that the SNR can be further increased without causing charge overflow at the input node of CCII, external amplifiers (Texas Instruments, OPA455) were used to provide excitation voltages higher than 5 V [43]. Ideally, if there is no mismatch in mutual capacitances, this should allow the SNR to be increased by up to 33.9 dB because the input node of CCIIs are not saturated. In practice, because of mutual-capacitance mismatch and power fluctuations from the external amplifier, the SNR is increased by up to 23.9 dB. It should be noted that the excitation amplitudes used in this experimental may not be practical for a commercial design, but even with modest excitation amplitudes, meaningful SNR improvements can be obtained.

Table II shows a performance comparison with previous work. In ideal case, the ROIC provides a maximum charge overflow reduction of 33.9 dB, which is the highest value among the previous works. The proposed CTS achieves a frame rate of 2.93 kHz and SNRs of 41.7 dB (Φ = 1 mm) and 61.6 dB (Φ = 10 mm) with a 32-in 104 × 64 TSP. Compared to [27], the frame rate is reduced from 3.9 to 2.93 kHz because of the two-time higher FFT resolution. In trade for this reduction, the two-time higher FFT resolution doubles the

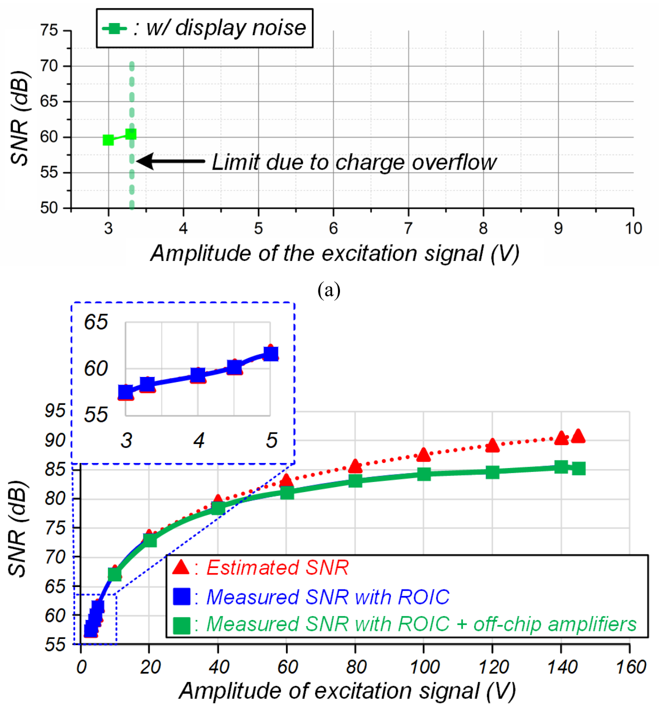

(a)

(b)

Fig. 16. Measured SNRs with display noise present (a) without and (b) with AM-MFE (f_d = 5.86 kHz).

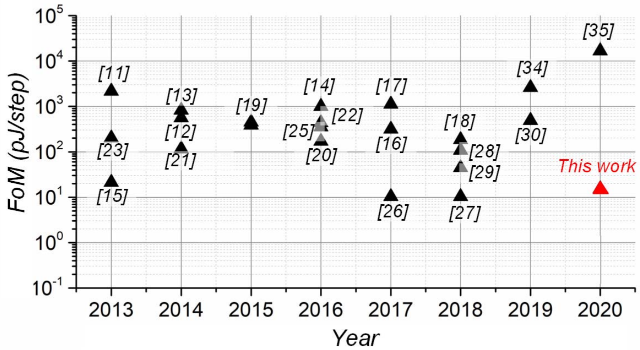

Fig. 17. FoM measurement of the ROIC with the prior art [43].

number of excitation frequencies, allowing them to be better located in the low noise region. Moreover, it also doubles the resolution with which pressure and tilt of an active stylus can be expressed [27].

Fig. 17 compares the figure-of-merit (FoM) [18] of the ROIC with the prior art. Using an excitation voltage of 5 V, the proposed ROIC achieves a FoM of 15.2 pJ/step, well below most of the prior art, and comparable to [26], [27]. When external amplifiers are used to generate higher excitation voltages, the FoM degrades to more than 100 pJ/step, in spite of the better SNR, due to the power consumption of the off-the-shelf external amplifiers. This may be improved in the future using more efficient on-chip high-voltage excitation circuits, which could be realized in a suitable high-voltage CMOS technology.

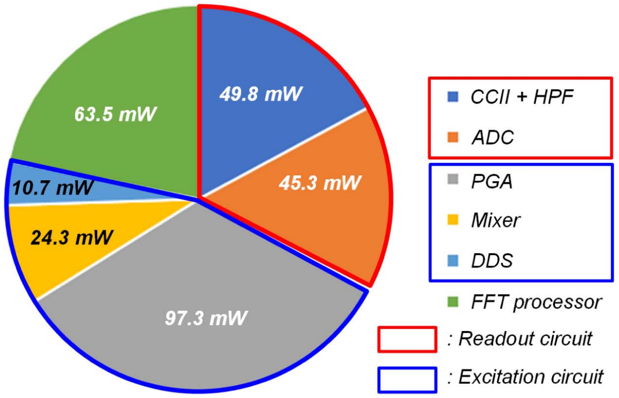

Fig. 18. Power breakdown of the ROIC.

Fig. 18 shows the power breakdown of the ROIC. In the ROIC, the readout circuit, excitation circuit, and FFT processor consume 95.1, 132, and 63.5 mW, respectively. The ROIC has a higher power consumption than most previous works because it includes an FFT processor, and a relatively large number of excitation and readout circuits. The power consumption of the digital part of the ROIC can be reduced by adopting a finer CMOS technology.

VI. CONCLUSION

This article has proposed an ROIC employing AM-MFE to prevent charge overflow. To prevent charge overflow, which occurs periodically at the beat frequency of the excitation frequencies, the ROIC modulates the amplitude of the excitation voltages at a frequency f_{MIX}, which is derived from the distribution of the excitation frequencies. Thus, the ROIC can sense the charge signal without charge overflow and maximize the SNR by increasing the excitation-signal amplitudes. In addition, the ROIC simultaneously drives all transmitter electrodes of the TSP, and thereby it achieves not only a high frame rate but also high SNR. The proposed ROIC has been fabricated in a 0.13-μm standard CMOS process, and measured with a 32-in 104 × 64 TSP using 1 and 10 mm metal pillars. When the excitation frequencies are assigned to have an equidistant and prime-number frequency spacing, the proposed ROIC using the AM-MFE reduces the charge overflow up to 33.9 dB, which is higher than previous works. In addition, the ROIC achieves a frame rate of 2.93 kHz, and SNRs of 41.7 and 61.6 dB when 1 and 10 mm metal pillars are used, respectively, making it suitable for high-end touch applications.

ACKNOWLEDGMENT

The authors would like to thank Mirae Nanotech, Cheongju, South Korea, for providing the 32-in TSP.

REFERENCES

[1] R. Adler and P. J. Desmares, "An economical touch panel using SAW absorption," *IEEE Trans. Ultrason., Ferroelectr., Freq. Control*, vol. UFFC-34, no. 2, pp. 195–201, Mar. 1987.
[2] D. Marioli, E. Sardini, and A. Taroni, "Ultrasonic distance measurement for linear and angular position control," *IEEE Trans. Instrum. Meas.*, vol. IM-37, no. 4, pp. 578–581, Dec. 1988.
[3] R. N. Aguilar and G. C. M. Meijer, "Fast interface electronics for a resistive touch-screen," in *Proc. IEEE Sensors*, Jun. 2002, pp. 1360–1363.

[4] J. Y. Han, “Low-cost multi-touch sensing through frustrated total internal reflection,” in *Proc. 18th Annu. ACM Symp. User interface Softw. Technol.*, Oct. 2005, pp. 115–118.

[5] *Fundamentals of Touch Technologies and Applications*. Accessed: Jul. 28, 2021. [Online]. Available: https://walkermobile.com/SID_2010_Short_Course_S4.pdf

[6] O.-K. Kwon, J.-S. An, and S.-K. Hong, “Capacitive touch systems with styli for touch sensors: A review,” *IEEE Sensors J.*, vol. 18, no. 12, pp. 4832–4846, Jun. 2018.

[7] S.-H. Lee, J.-S. An, S.-K. Hong, and O.-K. Kwon, “In-cell capacitive touch panel structures and their readout circuits,” in *Proc. 23rd Int. Workshop Active-Matrix Flatpanel Displays Devices (AM-FPD)*, Jul. 2016, pp. 258–261.

[8] I. S. Yang and O. K. Kwon, “A touch controller using differential sensing method for on-cell capacitive touch screen panel systems,” *IEEE Trans. Consum. Electron.*, vol. 57, no. 3, pp. 1027–1032, Aug. 2011.

[9] J.-S. An, S.-K. Hong, and O.-K. Kwon, “A highly linear and accurate touch data extraction algorithm based on polar coordinates for large-sized capacitive touch screen panels,” *IEEE Trans. Consum. Electron.*, vol. 62, no. 4, pp. 341–348, Nov. 2016.

[10] T.-H. Hwang, W.-H. Cui, I.-S. Yang, and O.-K. Kwon, “A highly area-efficient controller for capacitive touch screen panel systems,” *IEEE Trans. Consum. Electron.*, vol. 56, no. 2, pp. 1115–1122, May 2010.

[11] K. D. Kim *et al.*, “A capacitive touchscreen controller IC with noise-based hybrid sensing scheme,” in *SID Symp. Dig. Tech. Papers*, Jun. 2013, pp. 626–629.

[12] K.-D. Kim *et al.*, “A fully-differential capacitive touch controller with input common-mode feedback for symmetric display noise cancellation,” in *Symp. VLSI Circuits Dig. Tech. Papers*, Jun. 2014, pp. 1–2.

[13] Y.-S. Jang, Y.-H. Ko, J.-M. Choi, H.-S. Oh, and S.-G. Lee, “A 45-dB, 150-Hz, and 18-mW touch controller for on-cell capacitive TSP systems,” *IEEE Trans. Circuits Syst. II, Exp. Briefs*, vol. 61, no. 10, pp. 748–752, Oct. 2014.

[14] D.-H. Yeo, S.-H. Kim, H.-K. Noh, B. Kim, J.-Y. Sim, and H.-J. Park, “A SNR-enhanced mutual-capacitive touch-sensor ROIC using an averaging with three specific TX frequencies, a noise memory, and a compact delay compensation circuit,” *IEEE Sensors J.*, vol. 16, no. 18, pp. 6931–6938, Sep. 2016.

[15] S. Ko, H. Shin, H. Jang, I. Yun, and K. Lee, “A 70dB SNR capacitive touch screen panel readout IC using capacitor-less trans-impedance amplifier and coded orthogonal frequency-division multiple sensing scheme,” in *Proc. Symp. VLSI Circuits*, Kyoto, Japan, Jun. 2013, pp. C216–C217.

[16] S.-H. Park, H.-S. Kim, J.-S. Bang, G.-H. Cho, and G.-H. Cho, “A 0.26-nJ/node, 400-kHz Tx driving, filtered fully differential readout IC with parasitic RC time delay reduction technique for 65-in 169 × 97 capacitive-type touch screen panel,” *IEEE J. Solid-State Circuits*, vol. 52, no. 2, pp. 528–542, Feb. 2017.

[17] J.-S. An, S.-J. Jung, S.-K. Hong, and O.-K. Kwon, “A highly noise-immune capacitive touch sensing system using an adaptive chopper stabilization method,” *IEEE Sensors J.*, vol. 17, no. 3, pp. 803–811, Feb. 2017.

[18] H. Hwang, H. Lee, M. Han, H. Kim, and Y. Chae, “A 1.8-V 6.9-mW 120-fps 50-channel capacitive touch readout with current conveyor AFE and current-driven $\Delta\Sigma$ ADC,” *IEEE J. Solid-State Circuits*, vol. 53, no. 1, pp. 204–218, Jan. 2018.

[19] M. Miyamoto, M. Hamaguchi, and A. Nagao, “A 143 × 81 mutual-capacitance touch-sensing analog front-end with parallel drive and differential sensing architecture,” *IEEE J. Solid-State Circuits*, vol. 50, no. 1, pp. 335–343, Jan. 2015.

[20] S. Heo *et al.*, “72 dB SNR, 240 Hz frame rate readout IC with differential continuous-mode parallel architecture for larger touch-screen panel applications,” *IEEE Trans. Circuits Syst. I, Reg. Papers*, vol. 63, no. 7, pp. 960–971, Jul. 2016.

[21] H. Jang, H. Shin, S. Ko, I. Yun, and K. Lee, “12.5 2D Coded-aperture-based ultra-compact capacitive touch-screen controller with 40 reconfigurable channels,” in *IEEE Int. Solid-State Circuits Conf. (ISSCC) Dig. Tech. Papers*, Feb. 2014, pp. 218–219.

[22] J.-E. Park, J. Park, Y.-H. Hwang, J. Oh, and D.-K. Jeong, “11.6 A 100-TRX-channel configurable 85-to-385Hz-frame-rate analog front-end for touch controller with highly enhanced noise immunity of 20 Vpp,” in *IEEE Int. Solid-State Circuits Conf. (ISSCC) Dig. Tech. Papers*, Jan. 2016, pp. 210–211.

[23] H. Shin, S. Ko, H. Jang, I. Yun, and K. Lee, “A 55dB SNR with 240Hz frame scan rate mutual capacitor 30×24 touch-screen panel read-out IC using code-division multiple sensing technique,” in *IEEE Int. Solid-State Circuits Conf. (ISSCC) Dig. Tech. Papers*, Feb. 2013, pp. 388–389.

[24] M. Hamaguchi, A. Nagao, and M. Miyamoto, “12.3 A 240Hz-reporting-rate 143×81 mutual-capacitance touch-sensing analog front-end IC with 37dB SNR for 1 mm-diameter stylus,” in *IEEE Int. Solid-State Circuits Conf. (ISSCC) Dig. Tech. Papers*, Feb. 2014, pp. 214–215.

[25] C. Park *et al.*, “A pen-pressure-sensitive capacitive touch system using electrically coupled resonance pen,” *IEEE J. Solid-State Circuits*, vol. 51, no. 1, pp. 168–176, Jan. 2016.

[26] J.-S. An *et al.*, “9.6 A 3.9 kHz-frame-rate capacitive touch system with pressure/tilt angle expressions of active stylus using multiple-frequency driving method for 65’ 104×64 touch screen panel,” in *IEEE Int. Solid-State Circuits Conf. (ISSCC) Dig. Tech. Papers*, Feb. 2017, pp. 168–169.

[27] J.-S. An *et al.*, “A 3.9-kHz frame rate and 61.0-dB SNR analog front-end IC with 6-bit pressure and tilt angle expressions of active stylus using multiple-frequency driving method for capacitive touch screen panels,” *IEEE J. Solid-State Circuits*, vol. 53, no. 1, pp. 187–203, Jan. 2018.

[28] K.-H. Lee *et al.*, “A noise-immune stylus analog front-end using adjustable frequency modulation and linear-interpolating data reconstruction for both electrically coupled resonance and active styluses,” in *IEEE Int. Solid-State Circuits Conf. (ISSCC) Dig. Tech. Papers*, Feb. 2018, pp. 184–185.

[29] J.-S. An *et al.*, “Multi-way interactive capacitive touch system with palm rejection of active stylus for 86’ touch screen panels,” in *IEEE Int. Solid-State Circuits Conf. (ISSCC) Dig. Tech. Papers*, Feb. 2018, pp. 182–183.

[30] J.-E. Park, J. Park, Y.-H. Hwang, J. Oh, and D.-K. Jeong, “A Noise-Immunity-Enhanced analog front-end for 36 × 64 touch-screen controllers with 20-V_{PP} noise tolerance at 100 kHz,” *IEEE J. Solid-State Circuits*, vol. 54, no. 5, pp. 1497–1510, May 2019.

[31] M. Hamaguchi, M. Takeda, and M. Miyamoto, “6.6 A 240Hz-reporting-rate mutual-capacitance touch-sensing analog front-end enabling multiple active/passive styluses with 41dB/32dB SNR for 0.5 mm diameter,” in *IEEE Int. Solid-State Circuits Conf. (ISSCC) Dig. Tech. Papers*, Feb. 2015, pp. 1–3.

[32] J.-S. An, J.-H. Ra, E. Kang, M. A. P. Pertijs, and S.-H. Han, “28.1 A capacitive touch chipset with 33.9dB charge-overflow reduction using amplitude-modulated multi-frequency excitation and wireless power and data transfer to an active stylus,” in *IEEE Int. Solid-State Circuits Conf. (ISSCC) Dig. Tech. Papers*, Feb. 2020, pp. 430–431.

[33] H. Jang, H. Shin, J. Lee, C. Yoo, K. Chun, and I. Yun, “28.2 A 51dB-SNR 120Hz-scan-rate 32×18 segmented-VCOM LCD in-cell touch-display-driver IC with 96-channel compact shunt-sensing self-capacitance analog front-end,” in *IEEE Int. Solid-State Circuits Conf. (ISSCC) Dig. Tech. Papers*, Feb. 2020, pp. 432–433.

[34] Y.-H. Hwang *et al.*, “An always-on 0.53-to-13.4 mW power-scalable touchscreen controller for ultrathin touchscreen displays with current-mode filter and incremental hybrid $\Delta\Sigma$ ADC,” in *Proc. IEEE 45th Eur. Solid State Circuits Conf. (ESSCIRC)*, Sep. 2019, pp. 313–316.

[35] T.-G. Song, D.-K. Kim, J.-H. Cho, J.-H. Lee, and H.-S. Kim, “A 50.7dB-DR finger-resistance extractable multi-touch sensor IC achieving finger-classification accuracy of 97.7% on 6.7-inch capacitive touch screen panel,” in *Proc. IEEE Symp. VLSI Circuits*, Jun. 2020, pp. 1–2.

[36] H. T. Nicholas and H. Samueli, “An analysis of the output spectrum of direct digital frequency synthesizers in the presence of phase-accumulator truncation,” in *Proc. 41st Annu. Symp. Freq. Control*, May. 1987, pp. 495–502.

[37] K.-H. Baek, E. Merlo, M.-J. Choe, A. Yen, and M. Sahrling, “A 1.7GHz 3 V direct digital frequency synthesizer with an on-chip dac in 0.35μm SiGe BiCMOS,” in *IEEE Int. Solid-State Circuits Conf. (ISSCC) Dig. Tech. Papers*, Feb. 2005, pp. 114–587.

[38] T. Denison, K. Consoer, W. Santa, A.-T. Avestruz, J. Cooley, and A. Kelly, “A 2 μW 100 nV/rtHz chopper-stabilized instrumentation amplifier for chronic measurement of neural field potentials,” *IEEE J. Solid-State Circuits*, vol. 42, no. 12, pp. 2934–2945, Dec. 2007.

[39] N. Verma, A. Shoeb, J. Bohorquez, J. Dawson, J. Guttag, and A. P. Chandrakasan, “A micro-power EEG acquisition SoC with integrated feature extraction processor for a chronic seizure detection system,” *IEEE J. Solid-State Circuits*, vol. 45, no. 4, pp. 804–816, Apr. 2010.

[40] R. Hogervorst, J. P. Tero, R. G. H. Eschauzier, and J. H. Huijsing, “A compact power-efficient 3 V CMOS rail-to-rail input/output operational amplifier for VLSI cell libraries,” in *IEEE Int. Solid-State Circuits Conf. (ISSCC) Dig. Tech. Papers*, Feb. 1994, pp. 244–245, doi: 10.1109/ISSCC.1994.344656.

[41] J. K.-R. Kim and B. Murmann, “A 12-b, 30-MS/s, 2.95-mW pipelined ADC using single-stage class-AB amplifiers and deterministic background calibration,” *IEEE J. Solid-State Circuits*, vol. 47, no. 9, pp. 2141–2151, Sep. 2012.

[42] M. Pelgrom, *Analog-to-Digital Conversion*. New York, NY, USA: Springer, 2017, pp. 367–403.

[43] *OPA455 High-Voltage (150-V), Wide-Bandwidth (6.5-MHz), High Output Current (45-mA), Unity-Gain Stable Op Amp*, documentOPA455 SBOSA16 Datasheet, Texas Instruments, Oct. 2020.

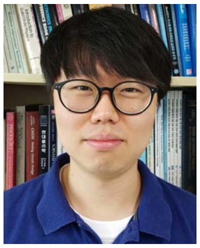

Jae-Sung An (Member, IEEE) received the B.S. and Ph.D. degrees from Hanyang University, Seoul, South Korea, in 2010 and 2018, respectively.

In 2018, he was with Leading UI Company, Ltd., Anyang, South Korea, where he developed the analog front-end ICs for the capacitive touch system and fingerprint sensing system. He joined the Electronic Instrumentation Laboratory, Delft University of Technology, Delft, The Netherlands, in 2018, where he was investigating the ultrasound imaging system. Since 2021, he has been working with Sony Semiconductor Solutions, Lysaker, Norway, to develop the automotive CMOS image sensors.

Jong-Hyun Ra received the B.S. degree in electronics and computer engineering from Hanyang University, Seoul, South Korea, in 2012.

Since 2012, he has been with the Integrated Electronics Laboratory, Hanyang University, where he researched the high-speed interface and digital logic design. In 2018, he was with SK Hynix, Icheon, South Korea, as a Researcher. His research area is a high-speed clock synthesis.

Eunchul Kang (Member, IEEE) received the B.S. and M.S. degrees in electronic engineering from Sogang University, Seoul, South Korea, in 2005 and 2007, respectively. He is currently pursuing the Ph.D. degree with the Electronic Instrumentation Laboratory, Delft University of Technology, Delft, The Netherlands.

From 2007 to 2010, he was with Fairchild Semiconductor, Bucheon, South Korea, as an Analog Design Engineer. He was a Research Assistant with the Inter-University Semiconductor Research Center, Seoul, from 2010 to 2011. He was a Design Engineer with Silicon Mitus, Seongnam, South Korea, with a focus on the design of power management ICs, from 2011 to 2015. Since 2020, he has been with Sony Semiconductor Solutions, Oslo, Norway, as a Senior Analog Design Engineer.

Michiel A. P. Pertijs (Senior Member, IEEE) received the M.Sc. and Ph.D. degrees (*cum laude*) in electrical engineering from the Delft University of Technology, Delft, The Netherlands, in 2000 and 2005, respectively.

From 2005 to 2008, he was with National Semiconductor, Delft, where he designed precision operational amplifiers and instrumentation amplifiers. From 2008 to 2009, he was a Senior Researcher with imec/Holst Centre, Eindhoven, The Netherlands. In 2009, he joined the Electronic Instrumentation Laboratory, Delft University of Technology, where he is currently an Associate Professor. He heads a research group focusing on integrated circuits for medical ultrasound and energy-efficient smart sensors. He has authored or coauthored two books, four book chapters, 15 patents, and over 120 technical articles.

Dr. Pertijs is a member of the technical program committee the European Solid-State Circuits Conference (ESSCIRC), and also served on the program committees for the International Solid-State Circuits Conference (ISSCC) and the IEEE Sensors Conference. He was a recipient of the ISSCC 2005 Jack Kilby Award for Outstanding Student Paper and the JSSC 2005 Best Paper Award. For his Ph.D. research on high-accuracy CMOS smart temperature sensors, he was a recipient of the 2006 Simon Stevin Gezel Award from the Dutch Technology Foundation STW. He served as an Associate Editor (AE) for the IEEE OPEN JOURNAL OF SOLID-STATE CIRCUITS (O-JSSC) and the IEEE JOURNAL OF SOLID-STATE CIRCUITS (JSSC). In 2014, he was elected as Best Teacher of the EE Program with the Delft University of Technology.

Sang-Hyun Han was born in Seoul, South Korea, in 1970. He received the B.S. degree in electronics engineering from Ajou University, Suwon, Gyeonggi-do, South Korea, in 1996.

He worked as a Researcher with the Samsung Electronics System LSI Division, Giheung-gu, Yongin-si, Gyeonggi-do. He is currently working for LeadingUI as a Chief Technology Officer (CTO). His major research areas are analog and digital mixed-circuit design and system-on-chip (SoC) architecture design.